

End2Reg: Learning Task-Specific Segmentation for Markerless Registration in Spine Surgery

Lorenzo Pettinari^{1*}, Sidaty El Hadramy¹, Michael Wehrli¹,
Philippe C. Cattin¹, Daniel Studer², Carol C. Hasler²,
Maria Licci²

¹Department of Biomedical Engineering, University of Basel, Allschwil, Switzerland.

²Department of Orthopedics, University Children's Hospital, Basel, Switzerland.

*Corresponding author(s). E-mail(s): lorenzo.pettinari@unibas.ch;

Abstract

Purpose: Intraoperative navigation in spine surgery demands millimeter-level accuracy. Current systems based on intraoperative radiographic imaging and bone-anchored markers are invasive, radiation-intensive and workflow disruptive. Recent markerless RGB-D registration methods offer a promising alternative, but existing approaches rely on weak segmentation labels to isolate relevant anatomical structures, which can propagate errors throughout registration.

Methods: We present End2Reg an end-to-end deep learning framework that jointly optimizes segmentation and registration, eliminating the need for weak segmentation labels and manual steps. The network learns segmentation masks specifically optimized for registration, guided solely by the registration objective without direct segmentation supervision.

Results: The proposed framework achieves state-of-the-art performance on ex- and in-vivo benchmarks, reducing median Target Registration Error by 32% to 1.83 mm and mean Root Mean Square Error by 45% to 3.95 mm, respectively. An ablation study confirms that end-to-end optimization significantly improves registration accuracy.

Conclusion: The presented end-to-end RGB-D registration pipeline removes dependency on weak labels and manual steps, advancing towards fully automatic, markerless intraoperative navigation. Code and interactive visualizations are available at: <https://lorenzopettinari.github.io/end-2-reg/>.

Keywords: Markerless registration, RGB-D point clouds, Intraoperative navigation, Spine surgery, End-to-end deep learning

1 Introduction

Intraoperative navigation systems have become integral to modern orthopedic surgery, where millimeter-level accuracy is often required to ensure both safety and clinical success [1]. This is particularly evident in pedicle screw insertion, where misplacement can lead to severe complications such as neural or vascular injury [2, 3]. The effectiveness of navigation systems is critically dependent on robust registration strategies that align image-derived anatomical information of the patient with the surgical coordinate system, allowing accurate instrument tracking and guidance [3, 4].

Anatomical information for registration can be obtained either intraoperatively or preoperatively. Preoperative imaging, such as computed tomography (CT) or magnetic resonance imaging (MRI), enables detailed surgical planning, including the selection of optimal implant sizes and insertion trajectories [4]. However, the preoperative plan must be accurately mapped onto the intraoperative anatomy to be effectively integrated in a navigation system. Current state-of-the-art navigation systems in orthopedics typically achieve this alignment through intraoperative 3D radiographic imaging in combination with bone-anchored fiducial markers [3, 5]. While effective, this strategy has notable drawbacks, as intraoperative radiographic imaging exposes patients and surgical staff to ionizing radiation, especially in multi-level procedures requiring repeated scans [6]. Furthermore, these systems are costly, occupy valuable operating room space, and prolong the workflow [7]. Bone-anchored markers are invasive and can loosen during surgery, necessitating repeated registrations [5].

To overcome these limitations, recent work has investigated radiation-free and markerless approaches, often using Red Green Blue - Depth (RGB-D) cameras to capture the surgically exposed intraoperative surface and register it to preoperatively acquired images [8–11]. RGB-D sensors are a compact, low-cost alternative and can be easily integrated into the operating room. RGB-D frames are converted into 3D point clouds, while preoperative CT or MRI scans are segmented to extract the anatomy of interest. The segmented volumes are converted into meshes (e.g., via Marching Cubes) and sampled to obtain point clouds of e.g. the spine. Registration is then formulated as a point cloud alignment problem between preoperative and intraoperative data.

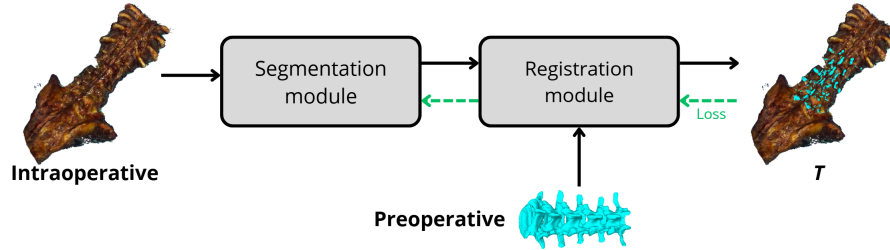


Fig. 1: Overview of the **End2Reg** network architecture, consisting of a segmentation and a registration module. The intraoperative RGB-D-derived point cloud and the preoperative mesh-derived point cloud are provided as inputs. The registration loss is backpropagated through both modules for joint optimization. The network outputs the rigid transformation T , aligning the preoperative model to the intraoperative scene.

This task is challenging due to the presence of soft tissue in intraoperative views and the limited visibility of exposed anatomy, which reduces geometric overlap with the preoperative model [8, 10, 12]. Moreover, point clouds obtained from RGB-D sensors differ from point clouds sampled from preoperative meshes in acquisition modality, resolution, and noise characteristics, and are often degraded by occlusions [8, 9].

Point cloud registration has been extensively studied [13]. Traditional methods include Iterative Closest Point (ICP) [14], which minimizes distances between points but is sensitive to initialization and low overlap, and Random Sample Consensus (RANSAC) [15] which is more robust to outliers and noise but computationally costly at high outlier rates. More recently, deep learning-based methods have improved accuracy and efficiency under challenging conditions such as partial overlap or complex transformations [13]. However, their application to point clouds from different imaging modalities in surgical contexts remains limited [16].

Existing work on RGB-D-based surgical registration in orthopedic surgery typically relies on ICP-based algorithms, supplemented by segmentation techniques to isolate bone structures from the surgically exposed surface [8–12, 17, 18]. When manual annotations are unavailable, these segmentations are generated from automatically created weak labels. The labels are produced by aligning the preoperative mesh with the intraoperative scene using ground-truth transformations, obtained either through manual alignment based on anatomical landmarks [10] or by intraoperative CT registration [8, 9, 11]. Labels are then assigned based on point-to-mesh distances [10, 18]. Alternatively, segmentation can be defined in the RGB domain by projecting the aligned preoperative mesh onto the camera frame [8, 9, 11]. Although effective for large-scale data generation, these labels are inherently noisy and may propagate errors into the registration pipeline [18]. Furthermore, to address limited overlap between preoperative and intraoperative data, preoperative meshes are often pre-segmented into expected regions of exposure, introducing a manual step that adds variability and operator dependence [8, 9, 12, 17].

In this work, we propose End2Reg, a deep learning registration framework designed to overcome the limitations of previous approaches. Our main contributions are:

1. **Joint learning of segmentation and registration:** segmentation and registration are trained end-to-end without segmentation labels, allowing the network to learn task-specific segmentations optimized for registration.
2. **Registration of complete preoperative anatomy:** no need for manual pre-selection of regions expected to overlap, reducing operator-dependent variability.
3. **SOTA registration accuracy and robustness:** validated on SpineDepth [19] and SpineAlign [10], showing robustness to occlusions and viewpoint variations.

2 Method

To overcome the limitations of existing approaches discussed above, we propose **End2Reg** a deep learning-based framework that enables **end-to-end learning of segmentation and registration**. Our approach learns a task-specific segmentation optimized directly for registration, eliminating the need for explicit segmentation labels.

A central challenge in designing an end-to-end segmentation-registration framework is that the segmentation module must produce discrete segmentation masks, which introduces two sources of non-differentiability: (i) sampling from the categorical distribution predicted by the segmentation module for each point in the input point cloud, and (ii) applying the argmax to obtain hard one-hot labels. Both operations block gradient backpropagation, preventing joint optimization of segmentation and registration. We address these challenges by combining the **Gumbel-Softmax reparameterization** [20], which provides a differentiable approximation of categorical sampling, with a **Straight-Through Estimator (STE)** [21], which allows gradients to flow through the argmax operation during training. An overview of the complete architecture is shown in Figure 1. The segmentation module, registration module, and end-to-end training strategy are described in the following subsections.

Segmentation Module

The segmentation module processes an intraoperative RGB-D point cloud, where each point is defined by its 3D coordinates and normalized RGB color values. Its objective is to produce a per-point labeling that identifies the relevant regions for registration. The module is built upon KPConv [22], and the architecture follows a symmetric U-Net-like encoder-decoder structure with skip connections, consisting of 5 stages (kernel size 15, initial voxel size 0.04, base radius 2.5). A final linear layer outputs per-point segmentation logits, which are converted into a segmentation mask. This mask serves as the feature input for the subsequent registration module.

Registration Module

The registration module takes preoperative and intraoperative point clouds as input and predicts a rigid transformation aligning them. Preoperative points are assigned a constant feature of 1, while intraoperative points receive a single binary feature derived from the segmentation mask. This module is based on GeoTransformer [23]. A KPConv network, similar to the one used in the segmentation module, acts as a shared encoder-decoder for both inputs, with three downsampling stages (kernel size 20, initial voxel size 0.025, base radius 7.0) and corresponding upsampling stages with skip connections. At the bottleneck of the KPConv encoder, the point cloud is downsampled into superpoints, representing the original cloud at a coarser resolution. Coarse correspondences between superpoints are estimated first and then refined using the dense per-point descriptors from the decoder, resulting in the final rigid transformation.

End-to-End Training

A key challenge in our framework arises from the discrete nature of segmentation masks. For each point $j \in \{1, \dots, N\}$ of the intraoperative point cloud, the segmentation module outputs logits $\mathbf{z}_j = [z_{j0}, z_{j1}]$ for two classes (relevant vs. irrelevant). Applying a softmax yields class probabilities $\boldsymbol{\pi}_j = \text{softmax}(\mathbf{z}_j)$. From these probabilities, a binary segmentation mask is derived as $\mathbf{Y} = [Y_1, \dots, Y_N]$, where each $Y_j \in \{0, 1\}$ denotes the predicted label of point j . Computing this mask by either taking the maximum probability class for each point (arg max) or thresholding the probabilities results

in a deterministic assignment, **which is non-differentiable**. As a result, **gradients from the registration loss cannot propagate through the segmentation module**, preventing it from learning task-specific features.

To enable end-to-end training, we adopt the **Gumbel-Softmax estimator** [20], which provides a differentiable approximation of categorical sampling via the Gumbel-Max trick. Specifically, by adding i.i.d. noise $g_{ji} \sim \text{Gumbel}(0, 1)$ to each logit z_{ji} , we obtain $Y_j = \arg \max_i (z_{ji} + g_{ji})$, which is a single sample drawn from the categorical distribution defined by π_j . Directly backpropagating through \mathbf{Y} is not possible because $\arg \max$ is non-differentiable. Therefore, we introduce a differentiable relaxation of the categorical sample using the Gumbel-Softmax distribution:

$$\tilde{y}_{ji} = \frac{\exp((z_{ji} + g_{ji})/\tau)}{\sum_{c=0}^1 \exp((z_{jc} + g_{jc})/\tau)}, \quad i \in \{0, 1\}, \quad j = 1, \dots, N \quad (1)$$

where $\tau > 0$. Unlike \mathbf{Y} , $\tilde{\mathbf{y}}$ is **continuous and differentiable with respect to \mathbf{z}** . As $\tau \rightarrow 0$, $\tilde{\mathbf{y}}$ converges in distribution to a one-hot vector, recovering categorical samples; for larger τ , it produces smoother values. To combine the discrete behavior of \mathbf{Y} with the differentiability of $\tilde{\mathbf{y}}$, we employ the **Straight-Through Gumbel-Softmax Estimator (ST-GS)** [20, 21], as illustrated in Figure 2.

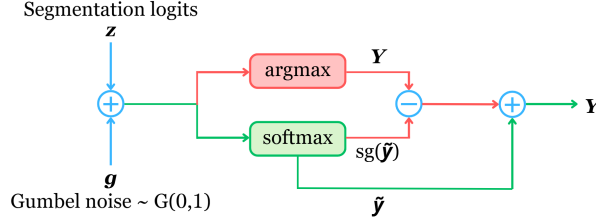


Fig. 2: Straight-Through Gumbel-Softmax Estimator (ST-GS). **Forward pass:** the one-hot vector \mathbf{Y} is obtained from logits \mathbf{z} perturbed with Gumbel noise \mathbf{g} via $\arg \max$. **Backward pass:** gradients are computed through softmax $\tilde{\mathbf{y}}$, enabling end-to-end learning while preserving discrete forward computation. Fig. inspired by Wei *et al.* [24].

To implement the ST-GS, we follow the standard **Straight-Through Estimator** [21] formulation:

$$\mathbf{Y}_{\text{STE}} = \mathbf{Y} - \text{sg}(\tilde{\mathbf{y}}) + \tilde{\mathbf{y}}. \quad (2)$$

where $\text{sg}(\cdot)$ denotes the stop-gradient operator, which treats its input as a constant during backpropagation. In the **forward pass**, $\mathbf{Y}_{\text{STE}} = \mathbf{Y}$, because $\tilde{\mathbf{y}} - \text{sg}(\tilde{\mathbf{y}}) = 0$, so the network uses a hard class label for each point. During **backpropagation**, the gradient of \mathbf{Y}_{STE} with respect to \mathbf{z} is approximated using the differentiable $\tilde{\mathbf{y}}$:

$$\frac{\partial \mathbf{Y}_{\text{STE}}}{\partial \mathbf{z}} = \frac{\partial (\mathbf{Y} - \text{sg}(\tilde{\mathbf{y}}) + \tilde{\mathbf{y}})}{\partial \mathbf{z}} = \underbrace{\frac{\partial \mathbf{Y}}{\partial \mathbf{z}}}_{=0} - \underbrace{\frac{\partial \text{sg}(\tilde{\mathbf{y}})}{\partial \mathbf{z}}}_{=0} + \frac{\partial \tilde{\mathbf{y}}}{\partial \mathbf{z}} \approx \frac{\partial \tilde{\mathbf{y}}}{\partial \mathbf{z}}. \quad (3)$$

This combination ensures that the segmentation module produces discrete binary masks in the forward pass while remaining trainable end-to-end. Consequently, gradients from the registration loss can propagate through the segmentation module, allowing it to learn task-specific segmentations without explicit supervision.

Once the binary segmentation mask is obtained through ST-GS, it is used as the per-point input feature in the feature extraction stage of GeoTransformer, which, like the segmentation network, is built upon KPConv [22]. In the standard KPConv formulation, when no additional features are available, each point is initialized with a constant scalar feature equal to one. In this setting, the network relies solely on geometric relationships between neighboring points. We modify this initialization for the intraoperative point cloud by replacing the constant feature with the binary label $Y_i \in \{0, 1\}$ predicted for each point. Accordingly, the input feature of each point becomes $F(x_i) = Y_i$. The KPConv convolution at a query point x is then expressed as:

$$(F * g)(x) = \sum_{x_i \in \mathcal{N}_x} g(x_i - x) F(x_i), \quad (4)$$

where x_i denotes the position of a neighboring point, $F(x_i) = Y_i$ is the feature assigned to x_i , \mathcal{N}_x is the neighborhood of x , and $g(\cdot)$ is the KPConv kernel function. In this formulation, all points remain part of the geometry, but only those with $Y_i = 1$ contribute to the convolution output. Points labeled as irrelevant ($Y_i = 0$) do not propagate information through the convolution. This design ensures that the registration backbone focuses on geometrically relevant regions identified by the segmentation module.

Training Loss

The training is performed using the GeoTransformer [23] dual-phase loss, which combines a coarse matching loss $\mathcal{L}_{\text{coarse}}$ and a fine matching loss $\mathcal{L}_{\text{fine}}$.

$$\mathcal{L} = \mathcal{L}_{\text{coarse}} + \mathcal{L}_{\text{fine}}, \quad (5)$$

The coarse matching loss follows a metric learning formulation, encouraging embeddings of corresponding local regions (superpoints) across the two point clouds to be close in feature space, while pushing apart embeddings of non-corresponding regions. The fine matching loss then refines correspondences between superpoints through a point-to-point matching objective, ensuring precise alignment of the point clouds. This work applies this dual-phase loss to registration of intraoperative RGB-D and preoperative anatomical point clouds. The combination of coarse metric-learning-based matching and fine point-to-point refinement provides a robust framework for establishing correspondences across point clouds extracted from different modalities.

3 Experiments and Results

Datasets and Implementation Details

End2Reg was validated on two benchmark datasets for vertebral registration: SpineDepth [19] (ex vivo) and SpineAlign [10] (in vivo, limited surgical exposure),

enabling evaluation under both controlled and realistic conditions. Training was performed on an NVIDIA RTX 5090 GPU (32 GB) with a batch size of 1 and an initial learning rate of 10^{-4} , including a 10 000-iteration warm-up and cosine annealing decay. Inference required, on average, 0.62 s per case for SpineDepth and 0.45 s for SpineAlign. Training memory usage was, on average, 9.3 GB and 6.1 GB for the respective datasets.

SpineDepth Dataset - Ex Vivo

The SpineDepth dataset [19] (Figure 3) contains RGB-D recordings of pedicle screw placement procedures on ten human cadaver specimens, along with preoperative 3D vertebral models (L1-L5) reconstructed from CT. An optical tracking system obtained ground-truth vertebral poses relative to the RGB-D sensor. Following Liebmann *et al.* [8], we selected Specimens 2-9 for our experiments.

The surgically exposed surface was segmented for each frame using the SAM2 model [25], filtering out the background before reconstructing the 3D point cloud. Frames with severe occlusions caused by the surgeon blocking the field of view were discarded, while those with less than 50% occlusion were retained to reflect realistic intraoperative scenarios. Preoperative vertebrae (L1-L5) were merged into a unique combined mesh, framing the task as a rigid registration problem. Point clouds were normalized by scaling them to fit inside a unit sphere. Random rigid transformations were applied to the preoperative models to simulate anatomical misalignment (translations ≤ 0.1 in unit-sphere coordinates, rotations $\leq 45^\circ$). An expert surgeon manually annotated anatomical landmarks for each vertebra: the spinous process and the left and right transverse processes, following Liebmann *et al.* [8]. These annotations are used to compute the Target Registration Error (TRE). Evaluation was performed using 8-fold cross-validation.

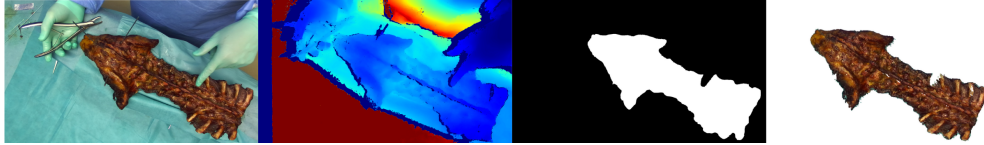


Fig. 3: Example from the SpineDepth dataset (cadaveric specimen). From left to right: RGB frame, depth frame, segmentation mask, exposed surface point cloud.

Registration results: Registration performance was evaluated using the TRE. Table 1 compares **End2Reg** with classical registration baselines (ICP, ICP+RANSAC), results reported by Liebmann *et al.* [8], and GMCNet [26] a deep learning-based architecture for partial-to-partial point cloud registration but without metric learning in its loss formulation. End2Reg achieves the lowest TRE, without requiring weak segmentation labels or manual selection of regions expected to overlap. Unlike prior work [8], we include frames with partial occlusions and use the full dataset without filtering based on viewpoint, providing a more realistic evaluation and demonstrating the framework’s robustness. GMCNet’s lower performance underlines the benefit of using metric learning in this context. Figure 4 shows registration results.

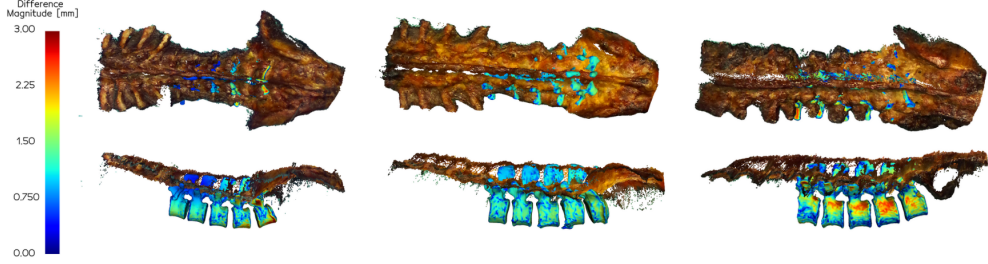


Fig. 4: End2Reg registration results of the preoperative mesh to the intraoperative RGB-D point cloud on **three different specimens**. Colors indicate the per-point displacement magnitude relative to the mesh transformed with the ground-truth pose.

Table 1: Registration result comparison on SpineDepth dataset: **TRE** median [1st quartile, 3rd quartile]. **No WSL**: no weak segmentation labels. **No MRS**: no manual region selection. **Part. Occ.**: partial occlusion included. **All view.**: all viewpoints included. **No M. Init.**: no manual registration initialization.

Method	No WSL	No MRS	Part. Occ.	All View.	No M. Init.	TRE [mm]
ICP	✗	✓	✓	✓	✓	11.00 [7.98, 20.58]
ICP	✗	✗	✓	✓	✓	5.42 [4.76, 7.22]
RANSAC+ICP	✗	✗	✓	✓	✓	4.20 [2.66, 6.66]
GMCNet [26]	✗	✓	✓	✓	✓	12.69 [9.48, 17.12]
Liebmann et al. [8]	✗	✗	✗	✗	✓	2.70 [1.70, 3.60]
End2Reg (Ours)	✓	✓	✓	✓	✓	1.83 [1.17, 2.70]

Unsupervised segmentation results: We evaluated the performance of the unsupervised segmentation module qualitatively. Figure 5 presents representative examples on different specimens. The results show that the model consistently separates bone from surrounding tissues, assigning label 1 to bone structures and label 0 to soft tissue.

SpineAlign Dataset - In Vivo

The SpineAlign dataset [10] comprises 24 lumbar spine surgeries acquired via an open posterior approach. Preoperative 3D vertebral meshes were generated from segmented CT or MRI scans. The dataset provides coarse alignment between preoperative meshes and intraoperative point clouds, based on at least three non-collinear anatomical landmarks identified by the surgeon. To simulate realistic surgical scenarios, occlusions are present in the recordings. Point clouds were preprocessed and preoperative misalignment simulated in the same way as for SpineDepth. For our experiments, 20 patients were used for training and 4 for testing using the same split as Daly *et al.* [10].

Registration results: Registration was evaluated using the RMSE, adopting the same protocol as Daly *et al.* [10]. We compared **End2Reg** against classical registration baselines (ICP, ICP+RANSAC), Daly *et al.* [10], and GMCNet [26]. As summarized

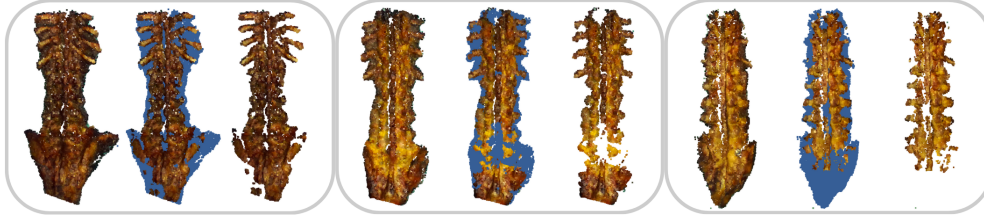


Fig. 5: Unsupervised segmentation results on **three different specimens**. For each, three point clouds are shown: intraoperative input point cloud, segmentation (label 0 in blue), and registration-relevant points (label 1). The selected points mainly correspond to bone structures, showing task-specific segmentation.

in Table 2, End2Reg achieves the lowest RMSE, outperforming all baselines without requiring segmentation labels or manual initialization. Consistent with the first dataset, GMCNet’s lower performance highlights the benefit of incorporating metric learning in the registration process.

Table 2: Registration result comparison on SpineAlign dataset: **RMSE** mean (\pm standard deviation). **No WSL**: no weak segmentation labels. **No MRS**: no manual region selection. **Part. Occ.**: partial occlusion included. **All view.**: all viewpoints included. **No M. Init.**: no manual registration initialization.

Method	No WSL	No MRS	Part. Occ.	All View.	No M. Init.	RMSE [mm]
ICP	✓	✓	✓	✓	✗	9.73 (± 5.56)
RANSAC + ICP	✓	✓	✓	✓	✗	8.41 (± 3.23)
GMCNet [26]	✓	✓	✓	✓	✓	9.95 (± 3.72)
Daly et al. [10]	✗	✓	✓	✓	✗	7.14 (± 0.47)
End2Reg (Ours)	✓	✓	✓	✓	✓	3.95 (± 1.76)

Unsupervised segmentation results: We qualitatively evaluated the unsupervised segmentation outputs on the SpineAlign dataset. Figure 6 shows results consistent with those on SpineDepth: the model autonomously highlights regions relevant for registration, which qualitatively correspond to bony anatomy.

Ablation Study: End-to-End Training

To evaluate the importance of the end-to-end training strategy, we performed an ablation study on the SpineDepth dataset, comparing our method with a two-step training using the same architecture. In the two-step training, the segmentation network was first trained with a cross-entropy loss using automatically generated weak labels. The weights of this network were then frozen, and only the registration network was subsequently trained. Ground-truth segmentation labels were derived from the preoperative mesh aligned with the ground-truth pose, assigning label 1 to intraoperative points within 3 mm of the surface [18]. Statistical analysis using the Wilcoxon signed-rank test



Fig. 6: Unsupervised segmentation on the SpineAlign dataset. From left to right: intraoperative point cloud, segmentation (label 0 in blue), and registration-relevant points (label 1).

on aggregated results from 8-fold cross-validation (Table 3) showed that end-to-end training significantly reduced TRE with a moderate effect size ($p \ll 0.05$, $r = 0.47$) and fewer outliers (3.8% vs. 7.0%), demonstrating the robustness of joint optimization.

Table 3: Comparison of TRE between the two-step training strategy and the proposed end-to-end approach. Values are reported as median and inter quartile range. Asterisks (*) indicate a statistically significant difference ($p \ll 0.05$).

Method	TRE [mm]
Two-step	2.18 [1.51, 3.36]
End-to-end (*)	1.83 [1.17, 2.70]

4 Conclusion

We presented **End2Reg**, an **end-to-end framework** for preoperative-to-intraoperative vertebral point cloud registration that achieves SOTA performance on SpineDepth (ex vivo) [19] and SpineAlign (in vivo) [10] datasets. Unlike traditional pipelines, our method does **not require segmentation labels** and automatically learns task-specific segmentations optimized for registration. It enables accurate alignment of the full preoperative anatomical model while remaining robust to occlusions and varying camera viewpoints.

Current limitations include the assumption of rigid-body transformations, which restricts correction of intraoperative pose changes for individual vertebrae. Evaluation is also constrained by the scarcity of in vivo datasets with precise ground-truth alignments. Future work will address intervertebral motion and broader in vivo validation. Our framework offers the potential to improve accuracy and automation of markerless intraoperative registration, facilitating integration into clinical workflows.

Declarations

Conflict of interest The authors have no competing interests to declare relevant to this article’s content.

References

- [1] Luther, N., Iorgulescu, J.B., *et al.*: Comparison of navigated versus non-navigated pedicle screw placement in 260 patients and 1434 screws: screw accuracy, screw size, and the complexity of surgery. *Clin. Spine Surg.* **28**(5), 298–303 (2015)
- [2] Gelalis, I.D., Paschos, N.K., *et al.*: Accuracy of pedicle screw placement: a systematic review of prospective in vivo studies comparing free hand, fluoroscopy guidance and navigation techniques. *Eur. spine j.* **21**(2), 247–255 (2012)
- [3] Karkenny, A.J., Mendelis, J.R., *et al.*: The role of intraoperative navigation in orthopaedic surgery. *JAAOS-J. Am. Acad. Orthop. Surg.* **27**(19), 849–858 (2019)
- [4] Floyd, E., Cohn, P., *et al.*: A review of preoperative planning technologies for spinal deformity correction. In: *Semin. in Spine Surg.*, vol. 32, p. 100787 (2020). Elsevier
- [5] Holly, L.T., Foley, K.T.: Intraoperative spinal navigation. *Spine* **28**(15S), 54–61 (2003)
- [6] Striano, B.M., Crawford, A.M., *et al.*: Intraoperative navigation increases the projected lifetime cancer risk in patients undergoing surgery for adolescent idiopathic scoliosis. *The Spine J.* **24**(6), 1087–1094 (2024)
- [7] Tonetti, J., Boudissa, M., *et al.*: Role of 3d intraoperative imaging in orthopedic and trauma surgery. *Orthop. & Traumatol.: Surg. & Res.* **106**(1), 19–25 (2020)
- [8] Liebmann, F., Atzigen, M., *et al.*: Automatic registration with continuous pose updates for marker-less surgical navigation in spine surgery. *Med. Image Anal.* **91**, 103027 (2024)
- [9] Hu, X., Nguyen, A., Baena, F.R.: Occlusion-robust visual markerless bone tracking for computer-assisted orthopedic surgery. *IEEE Trans. on Instrum. and Meas.* **71**, 1–11 (2021)
- [10] Daly, C., Marconi, E., *et al.*: Towards markerless intraoperative tracking of deformable spine tissue. *arXiv preprint arXiv:2506.23657* (2025)
- [11] Liu, H., Baena, F.R.Y.: Automatic markerless registration and tracking of the bone for computer-assisted orthopaedic surgery. *IEEE Access* **8**, 42010–42020 (2020)
- [12] Zhu, S., Zhao, Z., Pan, Y., Zheng, G.: Markerless robotic pedicle screw placement based on structured light tracking. *Int. J. of Comput. Assist. Radiol. and Surg.* **15**(8), 1347–1358 (2020)
- [13] Lyu, M., Yang, J., *et al.*: Rigid pairwise 3d point cloud registration: A survey. *Pattern Recognit.* **151**, 110408 (2024)

- [14] Besl, P.J., McKay, N.D.: Method for registration of 3-d shapes. In: Sensor Fusion IV: Control Paradigms and Data Structures, vol. 1611, pp. 586–606 (1992). Spie
- [15] Fischler, M.A., Bolles, R.C.: Random sample consensus: a paradigm for model fitting with applications to image analysis and automated cartography. *Commun. of the ACM* **24**(6), 381–395 (1981)
- [16] Weber, M., Wild, D., *et al.*: Deep learning-based point cloud registration for augmented reality-guided surgery. In: 2024 IEEE Int. Symp. on Biomed. Imaging (ISBI), pp. 1–5 (2024). IEEE
- [17] Ji, S., Fan, X., *et al.*: Patient registration using intraoperative stereovision in image-guided open spinal surgery. *IEEE Trans. on Biomed. Eng.* **62**(9), 2177–2186 (2015)
- [18] Warner, W.R., Bhattacharya, I., *et al.*: Sparse-xm: Spine pose adjustment with rgb-d bone segmentation via cross-modality label transfer. In: Proc. of Med. Image Comput. and Compu. Assist. Interv. – MICCAI 2025, vol. LNCS 15968, pp. 532–541. Springer, Switzerland (2025)
- [19] Liebmann, F., Stütz, D., *et al.*: Spinedepth: a multi-modal data collection approach for automatic labelling and intraoperative spinal shape reconstruction based on rgb-d data. *J. of Imaging* **7**(9), 164 (2021)
- [20] Jang, E., Gu, S., Poole, B.: Categorical reparameterization with gumbel-softmax. *arXiv preprint arXiv:1611.01144* (2016)
- [21] Bengio, Y., Léonard, N., Courville, A.: Estimating or propagating gradients through stochastic neurons for conditional computation. *arXiv preprint arXiv:1308.3432* (2013)
- [22] Thomas, H., Qi, C.R., *et al.*: Kpconv: Flexible and deformable convolution for point clouds. In: Proc. of the IEEE/CVF Int. Conf. on Comput. Vis., pp. 6411–6420 (2019)
- [23] Qin, Z., Yu, H., *et al.*: Geotransformer: Fast and robust point cloud registration with geometric transformer. *IEEE Trans. on Pattern Anal. and Mach. Intell.* **45**(8), 9806–9821 (2023)
- [24] Wei, T., Patel, Y., *et al.*: Generalized differentiable ransac. In: Proc. of the IEEE/CVF Int. Conf. on Comput. Vis., pp. 17649–17660 (2023)
- [25] Ravi, N., Gabeur, V., *et al.*: Sam 2: Segment anything in images and videos. *arxiv* 2024. *arXiv preprint arXiv:2408.00714*
- [26] Pan, L., Cai, Z., Liu, Z.: Robust partial-to-partial point cloud registration in a full range. *IEEE Robot. and Autom. Lett.* **9**(3), 2861–2868 (2024)